

Coupling acid catalysis and selective oxidation over $\text{MoO}_3\text{-Fe}_2\text{O}_3$ for chemical looping oxidative dehydrogenation of propane

Received: 24 August 2022

Accepted: 31 March 2023

Published online: 11 April 2023

Check for updates

Xianhui Wang^{1,2,3,5}, Chunlei Pei^{1,2,3,5}, Zhi-Jian Zhao^{1,2,3,5}, Sai Chen^{1,2,3,4}, Xinyu Li^{1,2,3}, Jiachen Sun^{1,2,3}, Hongbo Song^{1,2,3}, Guodong Sun^{1,2,3,4}, Wei Wang^{1,2,3,4}, Xin Chang^{1,2,3}, Xianhua Zhang^{1,2,3,4} & Jinlong Gong^{1,2,3,4}✉

Redox catalysts play a vital role in chemical looping oxidative dehydrogenation processes, which have recently been considered to be a promising prospect for propylene production. This work describes the coupling of surface acid catalysis and selective oxidation from lattice oxygen over $\text{MoO}_3\text{-Fe}_2\text{O}_3$ redox catalysts for promoted propylene production. Atomically dispersed Mo species over $\gamma\text{-Fe}_2\text{O}_3$ introduce effective acid sites for the promotion of propane conversion. In addition, Mo could also regulate the lattice oxygen activity, which makes the oxygen species from the reduction of $\gamma\text{-Fe}_2\text{O}_3$ to Fe_3O_4 contribute to selectively oxidative dehydrogenation instead of over-oxidation in pristine $\gamma\text{-Fe}_2\text{O}_3$. The enhanced surface acidity, coupled with proper lattice oxygen activity, leads to a higher surface reaction rate and moderate oxygen diffusion rate. Consequently, this coupling strategy achieves a robust performance with 49% of propane conversion and 90% of propylene selectivity for at least 300 redox cycles and ultimately demonstrates a potential design strategy for more advanced redox catalysts.

Propylene is an important building block in the chemical industry^{1,2}. Due to the growing gap between the demand and supply of propylene produced from steam cracking and fluidized catalytic cracking (FCC) processes, on-purpose propylene production has attracted extensive attention^{3,4}. Non-oxidative propane dehydrogenation (PDH) has been implanted commercially over Pt- and Cr-based catalysts, but the propane conversion is restricted by thermodynamic equilibrium limitation^{5,6}. On the contrary, oxidative dehydrogenation (ODH) with different oxidants, such as air, oxygen, N_2O , or CO_2 , promotes propylene production. From the thermodynamic view, the oxidants consume hydrogen with a strongly exothermic reaction, which shifts the thermodynamic equilibrium toward the product of propylene^{7–9}. ODH process over Cr_2O_3 has been extensively investigated. Ab initio multiscale kinetic study is an effective strategy to theoretically understand

the reaction network and key intermediates^{8,10–12}. However, the propylene selectivity should be further improved, and the participation of oxidants like O_2 can potentially lead to explosion hazards.

Comparatively, chemical looping oxidative dehydrogenation (CL-ODH) is an effective strategy to address these challenges^{13–16}. Typically, the CL-ODH process is composed of dehydrogenation and regeneration reactors. In the dehydrogenation reactor, metal oxides, defined as redox catalysts, are reduced by propane. The reduced redox catalysts are subsequently re-oxidized in the regeneration reactor under air flow. Recently, a Mo-V-O mixed oxide for CL-ODH has been reported¹⁴. The dual-functional Mo-V-O presented a superior propylene production rate (6.9 mol $\text{C}_3\text{H}_6/\text{kg-cat/h}$) with 89% of propylene selectivity at 500 °C using the chemical looping technology. In addition to Mo-V-O, chemical looping also boosted ethylene production

¹School of Chemical Engineering & Technology, Key Laboratory for Green Chemical Technology of Ministry of Education, Tianjin University, 300072 Tianjin, China. ²Collaborative Innovation Center for Chemical Science & Engineering (Tianjin), 300072 Tianjin, China. ³Haihe Laboratory of Sustainable Chemical Transformations, 300192 Tianjin, China. ⁴Joint School of National University of Singapore and Tianjin University, International Campus of Tianjin University, 350207 Binhai New City, Fuzhou, China. ⁵These authors contributed equally: Xianhui Wang, Chunlei Pei, Zhi-Jian Zhao. ✉e-mail: jl.gong@tju.edu.cn

with over 90% of ethylene selectivity, employing alkali metal-promoted Mn-based¹⁵, perovskite¹³, and NiO-based redox catalysts¹⁶. The activity of different oxygen species has a major influence on oxidation reactions^{17,18}. Nonetheless, the volatilization and toxicity of vanadium oxide and the limited oxygen capacity of perovskite are still holdbacks.

Alternatively, economical and environmentally friendly Fe₂O₃ with high oxygen capacity singles out to be the desired candidate for industrial application^{19–21}. Fe₂O₃ hitherto was widely investigated in chemical looping processes, but few of the reports illustrated the CL-ODH process over Fe₂O₃ due to its limited catalytic performance in alkane dehydrogenation reaction^{22–24}. Moreover, Fe₂O₃ is inclined to over-oxidation without promoters^{22,25,26}. MoO₃ was widely studied for alkane dehydrogenation^{27–32}. The introduction of MoO₃ can be an effective strategy to graft extra active sites for propane activation. Furthermore, doping with higher valence metal cations (Mo⁶⁺) is an effective strategy to moderate the lattice oxygen activity¹⁴. Thus, Mo dopant plausibly promotes propane activation and modulates oxygen activity simultaneously. Novotný et al.²² prepared Fe₂O₃@MoO₃ oxides for ethane CL-ODH. Surface MoO_x-rich layer improved ethylene selectivity. However, ethane conversion deteriorated due to the formation of Fe₂(MoO₄)₃²². It would be advantageous to couple the alkane

activation ability from MoO₃ and the oxidation capacity from Fe₂O₃ for chemical looping oxidative dehydrogenation of propane.

Herein, we demonstrate the promotion of Mo dopant in Fe₂O₃-based redox catalysts for propane conversion via CL-ODH. Coupling the acid-catalytic ability from Mo dopant and mild lattice oxygen, MoO₃-Fe₂O₃ presented a higher surface exchange coefficient (1.6×10^{-4} cm/s) and moderate oxygen diffusion coefficient (6.7×10^{-9} cm²/s). Consequently, propylene productivity (9.6 mol C₃H₆/kg-cat/h) was greatly improved. As confirmed by aberration-corrected high-angle annular dark-field scanning transmission electron microscope (AC-HAADF-STEM), extended X-ray absorption fine structure (EXAFS), Raman, X-ray diffraction (XRD), and X-ray photoelectron spectroscopy (XPS), Mo atoms were atomically dispersed and enriched on the surface of as-synthesized redox catalysts. Subsequently, surface-enriched Mo cations induced great modification in acid properties, evidenced by NH₃ temperature-programmed desorption (NH₃-TPD) and diffused reflectance infrared Fourier transform spectroscopy (NH₃-DRIFTS). C₃H₈-D₂ temperature-programmed surface reaction (C₃H₈-D₂-TPSR) indicated that extra acid sites (Mo-OH) derived from isolated Mo atoms drastically promoted propane activation. Meanwhile, the Mo dopant effectively modified the lattice oxygen activity of the γ -Fe₂O₃ matrix. The dynamic change regarding the inhibited lattice oxygen

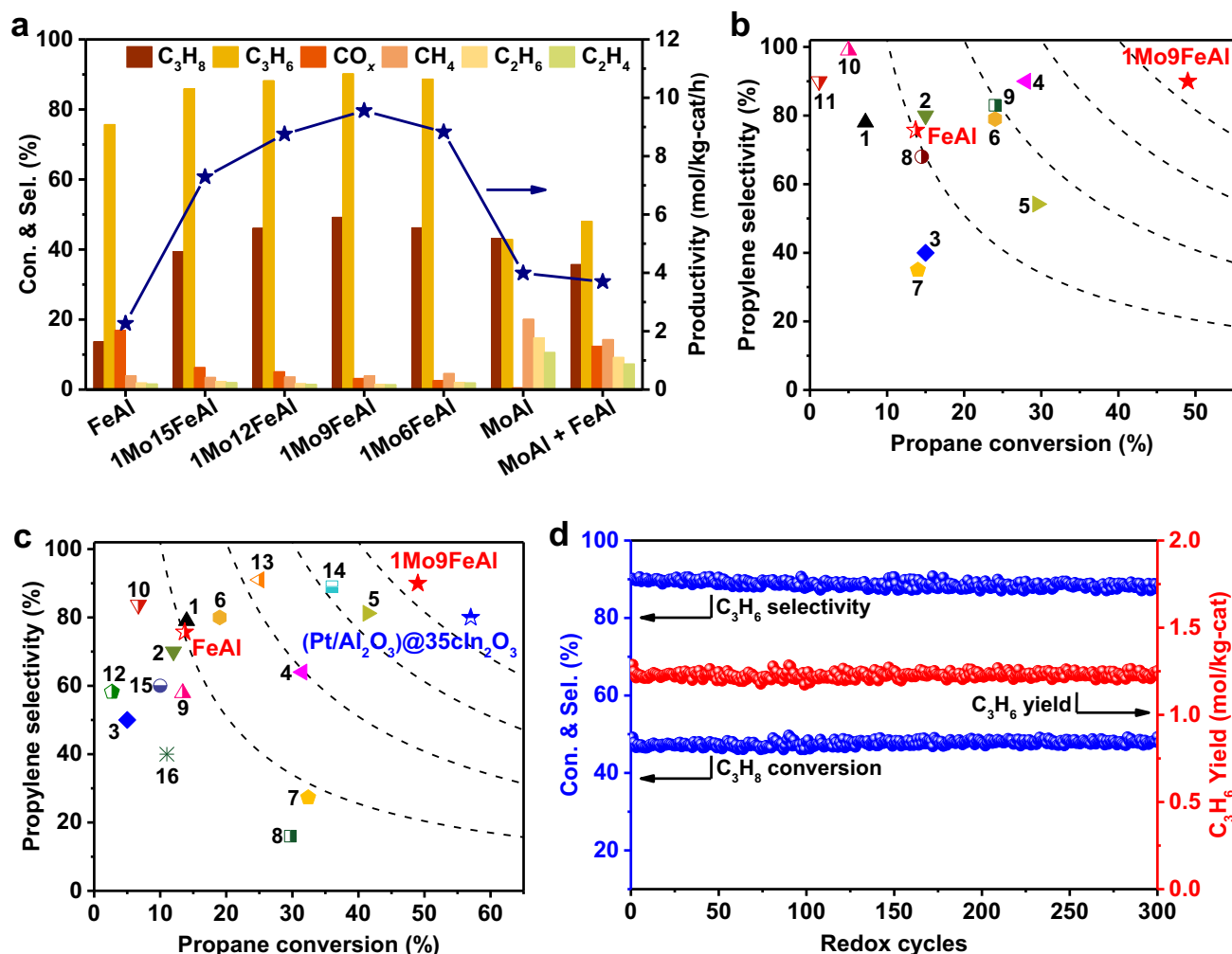


Fig. 1 | Catalytic performance and stability test. (a) Products distribution over different redox catalysts at the fourth minute, FeAl + MoAl represents the physical mixture of MoAl and FeAl. Comparison of 1Mo9FeAl with the catalytic performance of reported (b) Fe-based catalysts and (c) ODH catalysts. All referenced catalysts and citations are listed in Supplementary Tables 1 and 2. (d) Redox stability of

1Mo9FeAl in chemical looping oxidative dehydrogenation of propane. Reaction conditions: 570 °C, 0.14 MPa, GHSV = 3000 h⁻¹, 0.5 g sample, volumetric C₃H₈/N₂ ratio = 4:17. The identification of optimal reaction conditions is shown in Supplementary Fig. 1.

activity and alleviated oxygen out-diffusion was systematically studied by H₂ and C₃H₈ temperature-programmed reduction (H₂-TPR and C₃H₈-TPR), in situ DRIFTS, in situ Raman, and in situ XRD. Combining the kinetics experiments, thermal gravity (TG), C₃H₈ isothermal pulse and products distribution with time on stream, the coupling between acid catalysis, and selective oxidation was further confirmed.

Results

Dehydrogenation performance and redox stability test

In this work, a series of Al₂O₃-supported MoO₃-Fe₂O₃ with different molar ratios of Fe to Mo (1MoxFeAl, x = 15, 12, 9, 6) were synthesized via the conventional impregnation method. FeAl and MoAl were also prepared as references. See the “Methods” section for details.

As shown in Fig. 1a, Mo had a prominent influence on the performance of Fe₂O₃-based redox catalysts. At the oxidative dehydrogenation stage with minor CO_x (Supplementary Fig. 2)¹⁴, 1Mo9FeAl can reach up to 49% of propane conversion, 90% of propylene selectivity, and 98% of carbon balance or 9.6 mol C₃H₆/kg-cat/h for transient production rate at the fourth minute. The integral conversion and selectivity were determined to be 49% and 89% within 10 minutes (Supplementary Figs. 3 and 4). As summarized in Fig. 1b, c, the optimal 1Mo9FeAl presented comparable performance with that of (Pt/Al₂O₃)@35Cl₂O₃⁷. It also outperformed state-of-the-art Fe-based and other reported ODH catalysts. Comparatively, FeAl showed inferior performance in both propane conversion (14%) and propylene selectivity (76%), while the MoAl catalyst tended to cause cracking and carbon deposition. Therefore, more coke was burnt for the spent MoAl catalyst in comparison to 1Mo9FeAl in O₂ temperature-programmed oxidation (O₂-TPO) results (Supplementary Fig. 5). The physical mixture of MoAl and FeAl also presented inferior propylene selectivity, highlighting the formation of mixed metal oxides (MoO₃-Fe₂O₃). Meanwhile, the pre-reduced 1Mo9FeAl redox catalyst under H₂ flow (1Mo9FeAl-red) presented lower activity and propylene selectivity. The inferior performance emphasized the promotional effects of lattice oxygen for propylene production (Supplementary Fig. 6).

Cyclic stability is a significant evaluation criterion in the CL-ODH process. Redox experiments were carried out over 1Mo9FeAl (Fig. 1d). Propane conversion, propylene selectivity, and integral propylene yield kept stable for 300 redox cycles for 1Mo9FeAl, when the optimal regeneration time was 10 minutes (Supplementary Figs. 7 and 8)^{33–37}. In accordance with the robust redox stability, the XRD patterns and crystal sizes were consistent for fresh and regenerated redox catalysts (Supplementary Fig. 9 and Supplementary Table 3). Meanwhile, the molar ratio of Fe to Mo (Supplementary Fig. 10 and Supplementary Table 4) was constant for regenerated 1Mo9FeAl. The stable structure after multiple dehydrogenation-regeneration cycles led to stable performance. In summary, Mo dopant promoted both propane conversion and propylene selectivity in comparison to that of pristine FeAl. The improvement in propane conversion and propylene selectivity should be ascribed to the promoted propane activation and modification in lattice oxygen activity, respectively, and it will be discussed later. Meanwhile, the optimal 1Mo9FeAl redox catalyst presented a robust performance in the stability test, and the stable structure of the redox catalyst was favorable for its further application.

Textural properties

The textural properties of the redox catalysts were primarily characterized to illustrate the fine structure of 1MoxFeAl. The redox catalysts experienced one dehydrogenation-regeneration cycle and demonstrated a phase transformation from α-Fe₂O₃ (JCPDS 33-0664, hematite) to γ-Fe₂O₃ (JCPDS 39-1346, maghemite) according to XRD measurement^{36,37}, which were adopted for in-depth study (Supplementary Fig. 11). See the Supplementary Information for details. Basically, the Mo dopant had a minor effect on the surface area, pore volume, pore size distributions, and morphology because of the high

loading of γ-Fe₂O₃ (Supplementary Figs. 12 and 13, Supplementary Table 5).

AC-HAADF-STEM was employed to directly distinguish the location of Mo cations (Fig. 2a, Supplementary Fig. 14). Bright spots corresponding to isolated Mo atoms were detected in the Fe₂O₃ crystallites, despite the high density of Mo atoms. The isolation of Mo atoms was beneficial for propylene production since side reactions, such as cracking, were structure sensitive. EXAFS was further performed to confirm the isolation of Mo atoms. As shown in Fig. 2b and Supplementary Fig. 15, 1Mo9FeAl presented Mo-O coordination at around 1.80 Å without the appearance of Mo-Mo scattering paths, and the coordination number (CN) for Mo-O was determined to be about 4 (Supplementary Table 6)^{38,39}. The insignificant contribution of Mo-Mo scattering paths to the fitting data of 1Mo9FeAl from EXAFS results suggested the high dispersion of Mo atoms. Energy dispersive spectrometry (EDS) line scan in Supplementary Fig. 16 demonstrated that Mo atoms were in good coordination with the distribution of Fe element, indicating that Mo cations were primarily dispersed on Fe₂O₃ instead of Al₂O₃. Further increasing Mo content, Mo ensembles inevitably appeared in 1Mo6FeAl (Supplementary Fig. 17), which would catalyze the structure-sensitive side reactions and cause inferior propylene selectivity.

Due to the atomic dispersion of Mo atoms, FeAl and 1MoxFeAl presented typical characteristic peaks of γ-Fe₂O₃ without the appearance of MoO₃ (Fig. 2c)^{36,37}. The characteristic peaks were broader and weaker with increasing Mo content, implying the high dispersion of Mo cations. Furthermore, the characteristic peaks slightly shifted to a higher diffraction angle because of the smaller ionic radius of Mo⁶⁺ (0.59 Å) compared with that of Fe³⁺ (0.65 Å) (Supplementary Table 7)⁴⁰. The linear relationship between the peak shift and Mo contents indicated that Mo atoms were inserted into the γ-Fe₂O₃ matrix (Supplementary Fig. 18a). By contrast, the physical mixture of FeAl and MoAl exhibited identical characteristic peaks with that of FeAl (Supplementary Fig. 18b). Further increasing Mo content, Fe₂(MoO₄)₃ inevitably appeared for 1Mo3FeAl redox catalyst in the XRD pattern (Supplementary Fig. 19). As to MoAl catalyst (Supplementary Fig. 20), diffraction peaks ascribed to MoO₃ were not detected⁴¹.

Raman spectroscopy was also conducted to demonstrate the change in textual properties of 1MoxFeAl with Mo addition. FeAl and 1MoxFeAl exhibited exclusive resonant Raman peaks at 349–357, 502, 724 cm⁻¹, corresponding to T₂, E, A₁ vibrational modes of γ-Fe₂O₃ (Fig. 2d)^{42–44}. Identical to the XRD patterns, these peaks became weaker and broader, and the peak at 349 cm⁻¹ shifted to a higher Raman shift with enhanced Mo content. Meanwhile, Raman spectra of 1Mo6FeAl and 1Mo9FeAl presented a specific vibrational peak at 992 cm⁻¹ for Mo=O because of the distortion of [MoO₆] units and the intensity increased with Mo concentration^{25,45}. For 1Mo3FeAl, it exhibited peaks assigned to Fe₂(MoO₄)₃ at 965 and 780 cm⁻¹ (Supplementary Fig. 21), which was in accordance with the XRD patterns. Moreover, by comparison, Raman peaks at 815 and 875 cm⁻¹ corresponding to Al₂(MoO₄)₃ and peak at 965 cm⁻¹ ascribed to polymeric MoO_x were presented on MoAl and the physical mixture of MoAl and FeAl, but absent for 1Mo9FeAl in Supplementary Fig. 22^{31,32,46}. The difference in Raman spectra between FeAl, MoAl, and 1Mo9FeAl redox catalysts further demonstrated that Mo cations were located on γ-Fe₂O₃ instead of Al₂O₃.

Based on the above mentioned AC-HAADF-STEM, EXAFS, XRD, and Raman results, atomically dispersed Mo cations should be incorporated into the lattice of γ-Fe₂O₃ rather than dispersed on Al₂O₃ support. The isolation of Mo cations by surrounding γ-Fe₂O₃ matrix inhibited the appearance of Mo ensembles, which alleviated the structure-sensitive side reactions. However, further increasing Mo content, Mo ensembles and Fe₂(MoO₄)₃ unavoidably formed in 1Mo6FeAl and 1Mo3FeAl redox catalyst, respectively. Generally, γ-Fe₂O₃ acted well as a host for the atomic dispersion of Mo atoms.

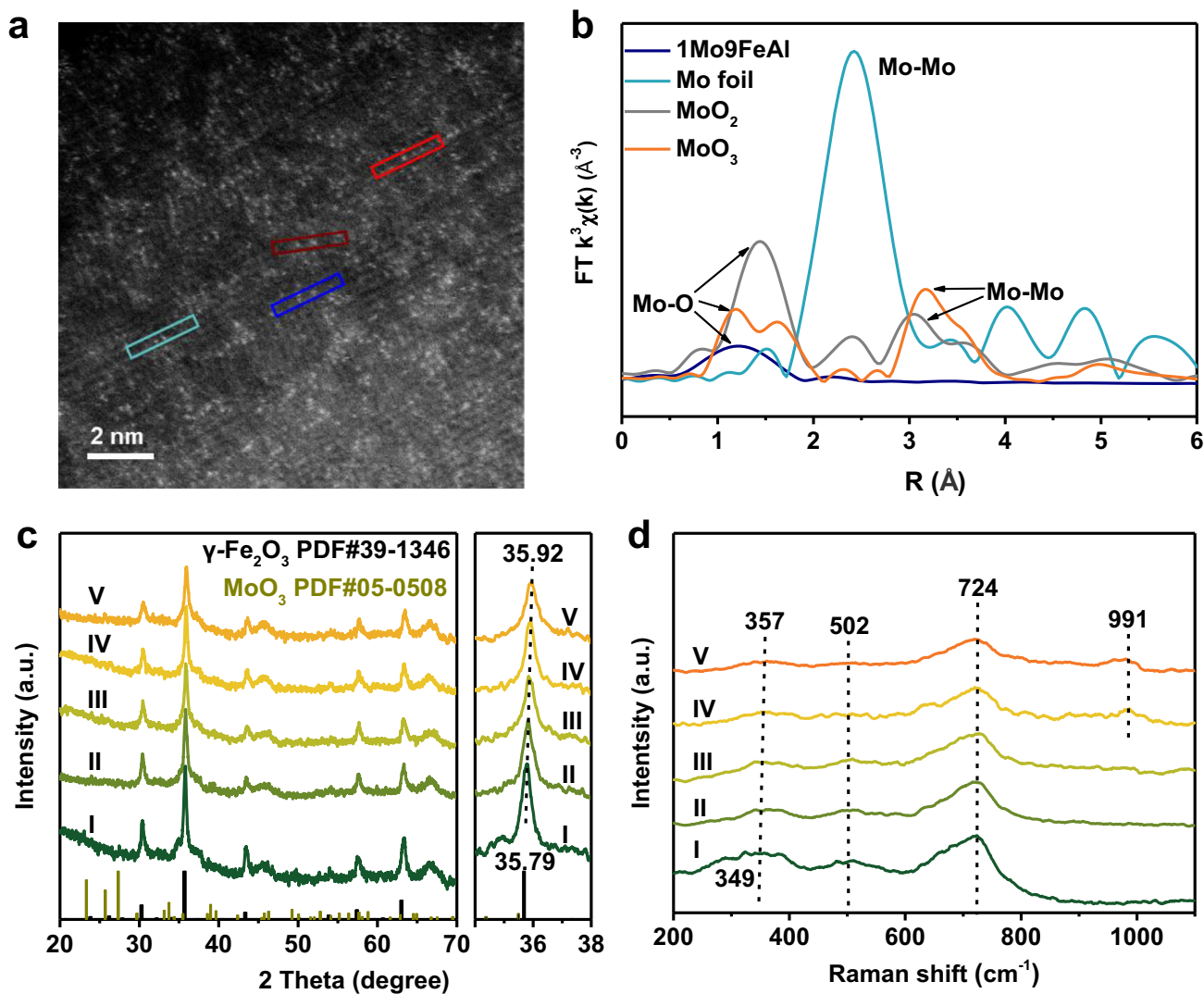


Fig. 2 | Morphology and textural properties of MoO₃-Fe₂O₃ redox catalysts. (a) AC-HAADF-STEM image of 1Mo9FeAl. (b) EXAFS spectra at Mo K-edge for 1Mo9FeAl, Mo foil, MoO₂, and MoO₃. XRD patterns (c) and Raman spectra (d) of

as-prepared redox catalysts. I, II, III, IV, and V are for FeAl, 1Mo15FeAl, 1Mo12FeAl, 1Mo9FeAl and 1Mo6FeAl, respectively. The a.u. stands for arbitrary units.

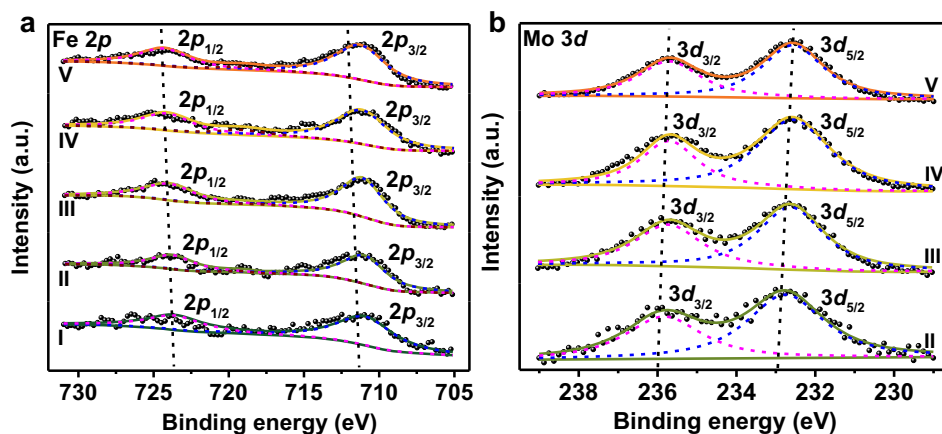


Fig. 3 | XPS measurements of MoO₃-Fe₂O₃ redox catalysts. XPS spectra for (a) Fe 2p, (b) Mo 3d of as-prepared redox catalysts. I, II, III, IV, and V are for FeAl, 1Mo15FeAl, 1Mo12FeAl, 1Mo9FeAl, and 1Mo6FeAl, respectively. The a.u. stands for arbitrary units.

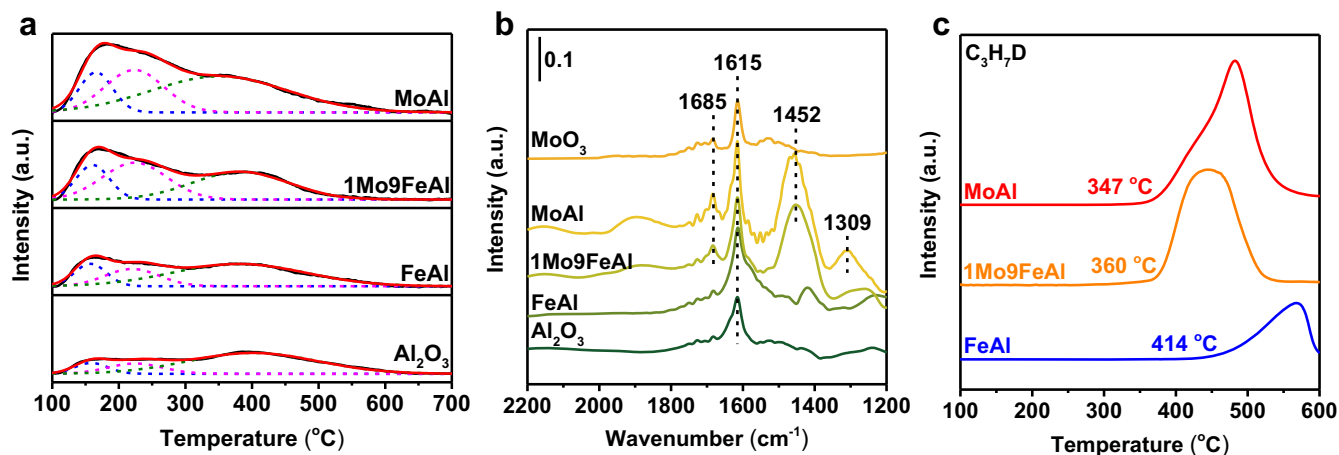


Fig. 4 | Modification on surface acid properties and its sequent promotion on propane activation. (a) NH₃-TPD profiles of Al₂O₃, FeAl, 1Mo9FeAl, and MoAl. NH₃-TPD was performed from 100 to 700 °C with a rate of 10 °C/min after being pre-treated in a flow of 5 vol% NH₃ in He (20 mL/min) for 1 h at 100 °C. (b) NH₃-DRIFTS

spectra of Al₂O₃, FeAl, 1Mo9FeAl, MoAl, and MoO₃. (c) Signal of C₃H₇D during C₃H₈-D₂-TPSR over FeAl, 1Mo9FeAl, and MoAl. The C₃H₈-D₂-TPSR experiments were conducted from 100 to 600 °C with a rate of 10 °C/min in a mixture of 5 vol% C₃H₈ and 5 vol% D₂ in He (10 mL/min). The a.u. stands for arbitrary units.

Mo accelerated surface reaction

The surface composition and chemical state of the redox catalysts were directly related to the improved performance for 1MoxFeAl. XPS experiments were performed accordingly.

Figure 3a and Supplementary Fig. 23 presented the XPS spectra of Fe 2*p*, and the peaks were centered at 710.9 and 724.3 eV, suggesting the emergence of separate Fe³⁺^{47,48}. Trivalent Fe cation was further verified by Fe K-edge X-ray absorption near-edge structure (XANES) spectra. FeAl and 1Mo9FeAl, with reference to γ-Fe₂O₃, presented similar curves in Fe K-edge XANES spectra, indicating the exclusive existence of Fe³⁺ in FeAl and 1Mo9FeAl redox catalyst (Supplementary Fig. 24). XPS spectra of Mo 3*d* shown in Fig. 3b demonstrated the exclusive existence of Mo⁶⁺ species^{27,29}. In accordance with previous literature²², Fe³⁺ shifted to higher binding energy, while Mo⁶⁺ shifted toward a lower value. However, Mo 3*d* spectra of MoAl shifted to a much higher binding energy. The back shift in binding energy for MoAl suggested the intimate interaction between Mo and γ-Fe₂O₃ in 1Mox-FeAl redox catalysts, supporting the peak shift in the XRD patterns and Raman spectra (Supplementary Fig. 25). Moreover, the derived surface composition shown in Supplementary Table 8 demonstrated that Mo cations took up a higher portion over the surface of 1MoxFeAl. The enrichment of Mo was beneficial for propane activation.

Obviously, Mo addition had a pronounced effect on the surface properties of redox catalysts. According to previous report²⁸, the surface acid properties directly affected the dehydrogenation reaction over Mo-based catalysts. NH₃-TPD was preliminary performed to detect the surface acid concentration. γ-Fe₂O₃ induced great modification in weak and medium acid sites in comparison to that of Al₂O₃. Twice the amount of weak and medium acid sites appeared for FeAl, while strong acid sites remained constant (Fig. 4a, Supplementary Table 9)^{49,50}. The introduction of Mo further increased acid site density. Especially, 1Mo9FeAl presented four times the amount of medium acid sites. However, MoAl presented twice the amount of strong acid sites, leading to severe side reactions and coke formation.

In addition to acid density, the introduction of Mo atoms also induced a significant modification on surface Lewis/Brønsted acid properties. As shown in Fig. 4b, Al₂O₃ and FeAl exhibited a single NH₃-adsorption peak at 1615 cm⁻¹, which was ascribed to Lewis acid sites, while new peaks at 1685 and 1452 cm⁻¹ ascribed to Brønsted acid emerged in 1Mo9FeAl and MoAl^{51–53}. Moreover, a specific peak at 1309 cm⁻¹ assigned to Lewis acid sites from the interaction of MoO species and Al₂O₃ support appeared for MoAl, which, however, was absent for 1Mo9FeAl^{54,55}. NH₃-DRIFTS for the physical mixture of MoO₃

and γ-Fe₂O₃ was also tested for comparison. The physical mixture presented NH₃-adsorption peaks at 1450 and 1683 cm⁻¹ for Brønsted acid despite that bulk MoO₃ and γ-Fe₂O₃ showed a separate Lewis acid at 1615 cm⁻¹ (Supplementary Fig. 26). Considering the XPS results that Fe and Mo cations were exclusively trivalent and hexavalent, -OH with negative electrons should be introduced on the charge-balancing sites created by the atomically Mo doping in Fe₂O₃ lattice to form Mo-OH. Mo-OH was then titrated as Brønsted acid sites in NH₃-DRIFTS experiments^{56,57}. The appearance of Brønsted acid for the physical mixture of MoO₃ and γ-Fe₂O₃ at 1450 cm⁻¹ and the absence of Lewis acid site at 1309 cm⁻¹ for 1Mo9FeAl further demonstrated that Mo atoms should be located over Fe₂O₃ for 1Mo9FeAl. Combining the above NH₃-DRIFTS results and the inferior propylene selectivity over the physical mixture of MoAl and FeAl, Mo-OH derived from Mo atoms isolated by γ-Fe₂O₃ should be responsible for the selective propylene production in 1Mo9FeAl.

The enrichment of Mo on the surface of 1MoxFeAl redox catalysts and its modulation of acid properties significantly promoted propane activation. As shown in the C₃H₈-D₂-TPSR results (Fig. 4c), propane was activated at 414 °C over FeAl redox catalyst, while the activation temperature was decreased to 360 °C under the promotion of Mo dopant. MoAl exhibited the best activation ability at 347 °C. The promoted propane activation conformed to the difference in catalytic performance that 1Mo9FeAl and MoAl presented a superior performance in propane conversion. In the dehydrogenation process, the stable acid properties (Supplementary Fig. 27) and Mo⁴⁺/Mo⁶⁺ ratio (11.7%, Supplementary Fig. 28a and Supplementary Table 10) provided constant catalytic sites for propane conversion. The consecutive out-diffusion of lattice oxygen from the reduction of Fe³⁺ to Fe²⁺ was the primary cause for the stabilization of Mo valence states (Supplementary Fig. 29). By contrast, much more Mo⁶⁺ was reduced to Mo⁴⁺ for the MoAl catalyst (23.2%) without consecutively out-diffused lattice oxygen (Supplementary Fig. 28b and Supplementary Table 11).

In summary, the introduction of the Mo atom had a prominent effect on the surface properties of the redox catalyst. Based on XPS spectra, Mo atoms were enriched on the surface of 1MoxFeAl redox catalysts. Meanwhile, surface-enriched Mo atoms significantly modified the acid properties of the redox catalysts. The Mo-OH derived from the Mo single atoms segregated by the γ-Fe₂O₃ matrix was the active site for propane activation. Because of the surface-enriched Mo cations and its modulation on acid properties, 1Mo9FeAl redox catalyst exhibited much better capacity in propane activation, as shown in the C₃H₈-D₂-TPSR results. In the dehydrogenation process, γ-Fe₂O₃ was

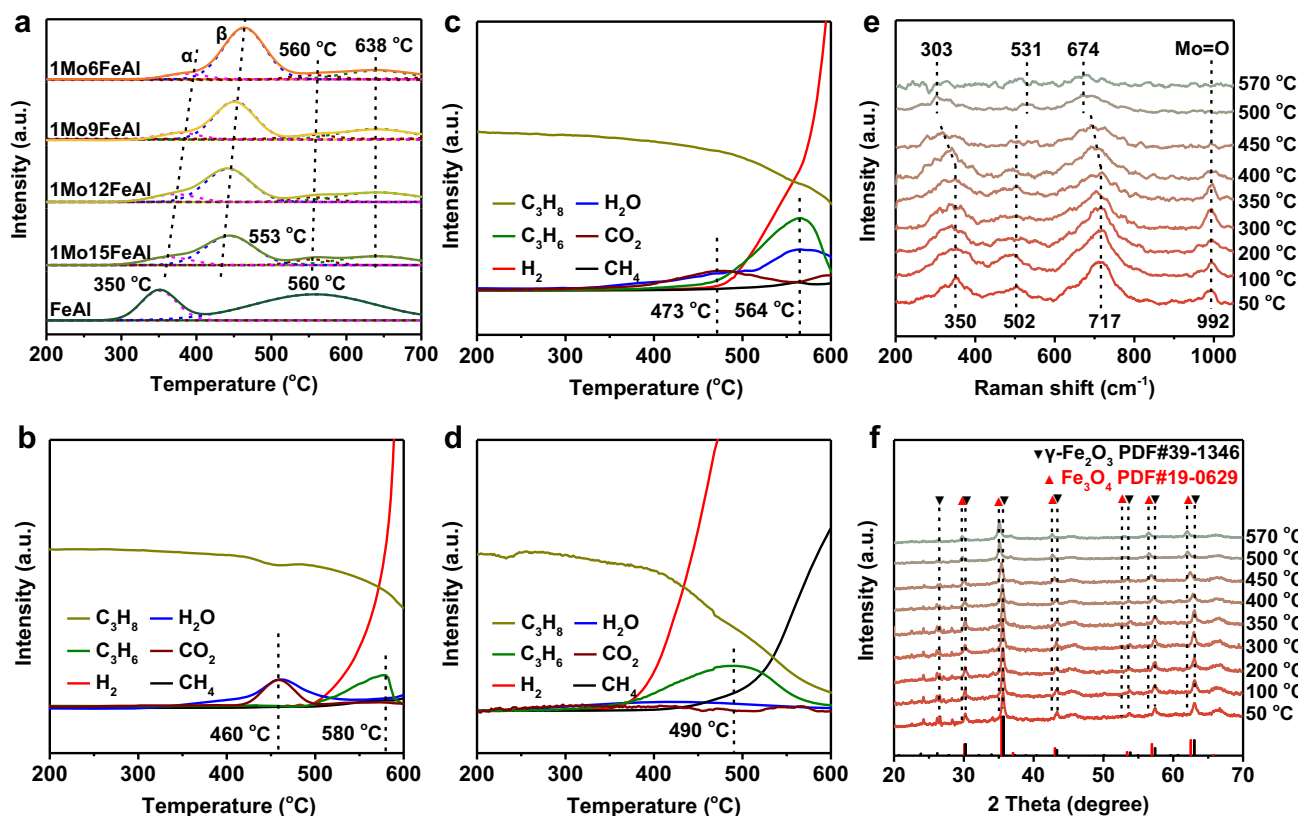


Fig. 5 | Modulation of overactive lattice oxygen species for $\text{MoO}_3\text{-Fe}_2\text{O}_3$ redox catalysts. (a) H_2 -TPR profiles of different redox catalysts ramping from 200 to 700 °C with a rate of 10 °C/min in a mixture of 10 vol% H_2 in Ar (30 mL/min). C_3H_8 -TPR mass spectra of (b) FeAl, (c) 1Mo9FeAl, (d) MoAl. The C_3H_8 -TPR experiments

were conducted from 200 to 600 °C with a rate of 10 °C/min in a mixture of 15 vol% C_3H_8 in He (10 mL/min). (e) In situ Raman spectra and (f) in situ XRD patterns of 1Mo9FeAl under the flow of 15 vol% C_3H_8 in He (20 mL/min) at different temperatures. The a.u. stands for arbitrary units.

gradually reduced and provided consecutively out-diffused lattice oxygen to stabilize the Mo valence state and consume the abstracted H species, promoting propylene production.

Mo modulated oxygen evolution

In addition to the accelerated surface reaction, the improved propylene selectivity and deteriorated CO_x content were directly related to the moderated lattice oxygen activity.

H_2 -TPR is a routine technique for evaluating the activity of different oxygen species. As shown in Fig. 5a, FeAl sample presented two typical reduction peaks as pure $\gamma\text{-Fe}_2\text{O}_3$ at 350 °C and 560 °C respectively. The reduction peak at 350 °C was corresponding to the reduction of $\gamma\text{-Fe}_2\text{O}_3$ to Fe_3O_4 , while the peak at 560 °C was the integrated results for the reduction of Fe_3O_4 to FeO and FeO to Fe^{38-61} . For 1MoxFeAl redox catalysts, the temperature for the first reduction peak was gradually increased with Mo content, and the asymmetric peak could be resolved into pairs (O_α and O_β). Considering the surface enrichment of Mo atoms and the low reduction temperature for MoAl (Supplementary Fig. 30), O_α was ascribed to the reduction of surface-enriched MoO_x , while O_β was corresponding to the reduction of $\gamma\text{-Fe}_2\text{O}_3$ to Fe_3O_4 . Based on the quantitative reduction temperature from H_2 -TPR (Supplementary Table 12), the reduction temperature for $\gamma\text{-Fe}_2\text{O}_3$ to Fe_3O_4 in 1Mo9FeAl was increased by 101 °C compared with that of FeAl.

The distinction of different oxygen species (O_α and O_β) was directly related to the products distribution in C_3H_8 -TPR results. For FeAl, oxygen species from the reduction of $\gamma\text{-Fe}_2\text{O}_3$ to Fe_3O_4 over-oxidized propylene to CO_2 and H_2O at 460 °C (Fig. 5b). Further increasing reduction temperature, propylene intensity reached a maximum value at 580 °C without CO_2 and H_2O , indicating the occurrence of non-oxidative dehydrogenation. However, the oxidative dehydrogenation

stage vanished for FeAl. Comparatively, 1Mo9FeAl presented a different C_3H_8 -TPR result (Fig. 5c). O_α devoted to over-oxidation with single pairs of CO_2 and H_2O at 473 °C, while O_β contributed to oxidative dehydrogenation with the production of C_3H_6 and H_2O at 564 °C. The increase in reduction temperature from $\gamma\text{-Fe}_2\text{O}_3$ to Fe_3O_4 between FeAl and 1MoxFeAl in H_2 -TPR results indicated the modification in lattice oxygen activity. Consequently, the original overactive oxygen species ($\gamma\text{-Fe}_2\text{O}_3$ to Fe_3O_4) in FeAl turned to be the moderate lattice oxygen (O_β) in 1Mo9FeAl for selectively oxidative dehydrogenation reaction. As to MoAl, propylene and H_2 appeared simultaneously in Fig. 5d with much lower CO_2 and H_2O signal intensity, indicating that the MoAl catalyst was primarily devoted to non-oxidative dehydrogenation.

To further examine the evolution of different oxygen species under reaction conditions, in situ Raman measurements were operated (Fig. 5e). At 50 °C, 1Mo9FeAl presented typical Raman peaks as $\gamma\text{-Fe}_2\text{O}_3$ ⁴²⁻⁴⁴. Peaks at 350 and 717 cm^{-1} shifted to the lower Raman shift with the consumption of lattice oxygen at dehydrogenation temperatures above 400 °C. Fe_3O_4 was ultimately formed at 500 °C with the appearance of new peaks at 303 and 674 cm^{-1} , indicating the controllable release of lattice oxygen⁶²⁻⁶⁵. Meanwhile, the complete disappearance of the peak located at 1409 cm^{-1} at 500 °C was also strong evidence for the phase transformation from $\gamma\text{-Fe}_2\text{O}_3$ to Fe_3O_4 (Supplementary Fig. 31). Besides the consumption of lattice oxygen from the reduction of $\gamma\text{-Fe}_2\text{O}_3$ to Fe_3O_4 , surface Mo=O was also depleted at 400 °C. The consumption of Mo=O in Raman spectra was identical to the in situ DRIFTS results that Mo=O presented a negative peak at 400 °C (Supplementary Fig. 32)^{66,67}. However, the consumed Mo=O can be replenished by the consecutively out-diffused lattice oxygen after regenerated at 570 °C under N_2 flow (Supplementary Fig. 33), which was in accordance with the stable Mo valence states in

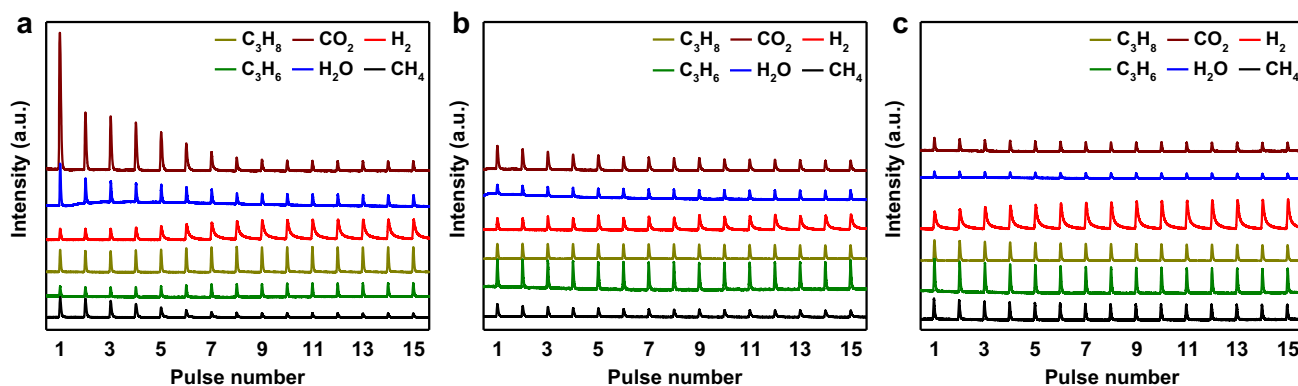


Fig. 6 | C_3H_8 pulses over $\text{MoO}_3\text{-Fe}_2\text{O}_3$ redox catalysts. Mass spectra during C_3H_8 pulses over **a** FeAl, **b** 1Mo9FeAl, and **c** MoAl; 0.5 mL of C_3H_8 was injected into the reactor for each pulse at 570 °C. The a.u. stands for arbitrary units.

XPS results for spent 1Mo9FeAl. Comparatively, phase transformation took place at 400 °C for FeAl, and the consumed lattice oxygen was supposed to deeply crack the produced propylene (Supplementary Fig. 31).

In situ XRD experiments presented comparable results to in situ Raman. 1Mo9FeAl and FeAl exhibited typical diffraction peaks corresponding to $\gamma\text{-Fe}_2\text{O}_3$ at dehydrogenation temperatures lower than 350 °C (Fig. 5f and Supplementary Fig. 34)^{36,37}. With the depletion of lattice oxygen, a phase transformation from $\gamma\text{-Fe}_2\text{O}_3$ to Fe_3O_4 suddenly occurred at 400 °C for FeAl^{33–35}. However, due to the moderate oxygen activity, the phase transformation terminated at 500 °C for 1Mo9FeAl, which was in correspondence with that in situ Raman spectra. Moreover, 1Mo9FeAl exhibited a superior ability for controllable oxygen release and prolonged oxidative dehydrogenation stage from the isothermal XRD patterns (Supplementary Fig. 35).

In summary, the Mo dopant effectively regulated the lattice oxygen activity in $\gamma\text{-Fe}_2\text{O}_3$. For FeAl, $\gamma\text{-Fe}_2\text{O}_3$ was reduced to Fe_3O_4 at 350 °C, and this specific oxygen species devoted to the over-oxidation of propylene. Oxygen species ascribed to the reduction of Fe_3O_4 was inert in oxidative dehydrogenation because of the high reduction temperature. With the addition of Mo atoms, MoO_x enriched on the surface was reduced at 400 °C (O_α) and contributed to over-oxidation, while the temperature for the reduction of $\gamma\text{-Fe}_2\text{O}_3$ to Fe_3O_4 for 1Mo9FeAl (O_β) was increased by 101 °C, which was then devoted to oxidative dehydrogenation. The increase in reduction temperature between FeAl and 1MoxFeAl in H_2 -TPR results induced a great modification in lattice oxygen activity. Consequently, the original over-active oxygen species ($\gamma\text{-Fe}_2\text{O}_3$ to Fe_3O_4) in FeAl devoted to selectively oxidative dehydrogenation reaction over 1Mo9FeAl.

Coupling effects of surface acid catalysis and selective oxidation

Based on the above catalytic performance and characterization results, isolated Mo atoms had a prominent influence on both the surface catalytic process and lattice oxygen activity for oxidative dehydrogenation. Atomically dispersed Mo atoms introduced abundant acid sites (Mo-OH) for propane conversion and passivated the lattice oxygen activity, matching the surface reaction and bulk oxygen diffusion to improve propylene selectivity. The coupling between surface acid catalysis and selective oxidation was further studied by kinetics experiments^{68,69}. The detailed calculation for the removal of external and internal mass transfer limitations can be found in the “Methods” section and Supplementary Table 13. The oxygen surface exchange coefficient, k , and bulk diffusion coefficient, D , shown in Supplementary Table 14, were calculated to quantify the surface reaction rate and lattice oxygen diffusion rate. Due to the promotion of surface acid sites, the surface reaction rate coefficient for 1Mo9FeAl (1.6×10^{-4} cm/s) was significantly accelerated, about an order of magnitude higher than that

of FeAl (1.2×10^{-5} cm/s). A high surface reaction rate coefficient resulted in much higher propane conversion, as shown in Fig. 1. Meanwhile, Mo dopant moderated lattice oxygen diffusion, leading to lower D value for 1Mo9FeAl (6.7×10^{-9} cm²/s) in comparison to that of FeAl (2.5×10^{-8} cm²/s), which significantly inhibited the over-oxidation and extended the oxidative dehydrogenation. Thermal gravity results in Supplementary Fig. 36 demonstrated comparable results. 1Mo9FeAl presented a slower oxygen release rate, which was in correspondence with the decreased D value. Furthermore, oxygen consumption was negligible for 1Mo9FeAl under C_3H_6 flow, while the oxygen consumption rate was twice for FeAl in C_3H_6 flow than in C_3H_8 flow. The contrast in lattice oxygen consumption rate under C_3H_6 flow between FeAl and 1Mo9FeAl further confirmed the superior propylene selectivity over 1Mo9FeAl redox catalyst.

Kinetics results were proved by the instantaneous composition in the outlet gas at different reaction times. Based on the CO_x concentration, the dehydrogenation progress was divided into three characteristic stages, over-oxidation, oxidative dehydrogenation, and non-oxidative dehydrogenation (Supplementary Fig. 37)¹⁴. The partition of the three distinctive regions was further proved by the propane isothermal reaction (Supplementary Fig. 38). Apparently, much more CO_x appeared in the exhausted gas of FeAl, and the over-oxidation stage was sustained for about 5 minutes. Furthermore, due to the high oxygen diffusion rate coefficient, or greater D value, the oxidative dehydrogenation region lasted for only 2 minutes. By contrast, 1Mo9FeAl presented satisfied CO_x selectivity at the second minute, and the oxidative dehydrogenation region lasted for at least 7 minutes, indicating moderate oxygen release or lower D value. Besides the prolonged oxidative dehydrogenation stage, the drastically improved propane conversion should be solid evidence for the increase in the k value. In summary, coupling the improved k , derived from enriched surface acid sites (Mo-OH) and decreased D , ascribed to the passivation in the out-diffusion of lattice oxygen, 1Mo9FeAl demonstrated good performance in chemical looping oxidative dehydrogenation of propane.

C_3H_8 isothermal pulse experiments were further performed to confirm the instantaneous composition of different products. As shown in Fig. 6a, FeAl was inclined to fully oxidize propylene in first several pulses, and the signal for H_2O and CO_2 was much higher than that of 1Mo9FeAl and MoAl. Consequently, it demonstrated 31% of CO_x selectivity in the first minute. In comparison to FeAl, 1Mo9FeAl could efficiently catalyze oxidative dehydrogenation (Fig. 6b), coupling surface acid catalysis and selective oxidation. 1Mo9FeAl presented higher propylene signal intensity, while the signal intensity for propane and CO_2 was much lower in the first few C_3H_8 pulses. Meanwhile, the signal for H_2 , H_2O , and C_3H_6 was rather stable with time on the stream, indicating the preservation of the oxidative dehydrogenation

stage. For the MoAl sample (Fig. 6c), the H₂ signal from non-oxidative dehydrogenation contributed dominantly to the exhausted gas. In accordance with the pulse experiments, H₂O/H₂ ratios over FeAl and 1Mo9FeAl also demonstrated the promotion of surface acid catalysis and oxidative dehydrogenation. As shown in Supplementary Fig. 39, FeAl presented a much higher H₂O/H₂ ratios from over-oxidation at the first few minutes. However, the H₂O/H₂ ratios were deteriorated in comparison to 1Mo9FeAl with the rapid depletion of lattice oxygen. For 1Mo9FeAl, O_β dominantly contributed to the selective oxidation, resulting in a stable H₂O/H₂ ratio and prolonged oxidative dehydrogenation period. Consequently, 46% of propylene was produced from the selective oxidative reaction in the CL-ODH process for 1Mo9FeAl at the fourth minute.

Discussion

An efficient MoO₃-Fe₂O₃ redox catalyst was designed for chemical looping oxidative dehydrogenation of propane. 1Mo9FeAl exhibited a superior performance with 49% of propane conversion and 90% of propylene selectivity for at least 300 cycles. Basically, atomically dispersed Mo cations enriched on the surface of 1Mo9FeAl redox catalyst introduced extra acid sites (Mo-OH), promoting propane conversion. Meanwhile, Mo cations effectively modulated lattice oxygen activity and out-diffusion rate, making the pristine over-reactive oxygen species available for selectively oxidative dehydrogenation. Due to the enhancement in surface acid sites and lattice oxygen modification upon isolated Mo doping, propylene production was significantly improved, coupling surface acid catalysis and selective oxidation. This study demonstrates the effects of surface acidity and lattice oxygen on selective dehydrogenation in chemical looping processes.

Methods

Catalysts preparation

Materials. Fe(NO₃)₃·9H₂O was purchased from Aladdin biological technology Co., Ltd. (Shanghai, China). (NH₄)₆Mo₇O₂₄·4H₂O was purchased from Tianjin yuanli chemical reagent Co., Ltd. (Tianjin, China). γ-Al₂O₃ was purchased from Adamas-beta reagent Co., Ltd. (Shanghai, China)

Synthesis of FeAl. Fe₂O₃/Al₂O₃ redox catalyst was defined as FeAl. FeAl was synthesized by a facile impregnation method, where γ-Al₂O₃ was employed as support, and Fe₂O₃ loading was fixed at 40 wt%. Typically, 3.367 g of Fe(NO₃)₃·9H₂O and 1 mL of deionized water were loaded in a 10-mL disposable centrifuge tube. Fe(NO₃)₃·9H₂O was dissolved in deionized water under ultrasound treatment for 1 h, forming a brown solution. The solution was then added to 1 g of γ-Al₂O₃ powder. The mixture was shaken on an oscillator and treated under ultrasound treatment for another 1 h. After impregnation, the brown slurry was dried at 100 °C for 12 h and then calcinated at 600 °C in a muffle furnace for 6 h.

Synthesis of 1MoxFeAl. Mo-doped Fe₂O₃/Al₂O₃ redox catalysts were defined as 1MoxFeAl, where x was the molar ratio of Fe to Mo (Fe/Mo, x = 6, 9, 12, 15). 1MoxFeAl was prepared by a simple co-impregnation process, where Fe₂O₃ loading was fixed at 40 wt%, while the amount of Mo was dependent on x value. Consequently, 0.2452, 0.1635, 0.1226, and 0.0981 g of (NH₄)₆Mo₇O₂₄·4H₂O (precursor of MoO₃) was added for the preparation of 1Mo6FeAl, 1Mo9FeAl, 1Mo12FeAl, and 1Mo15FeAl respectively. Typically, 3.367 g of Fe(NO₃)₃·9H₂O and the required amount of (NH₄)₆Mo₇O₂₄·4H₂O based on x value were loaded in a 10-mL disposable centrifuge tube in sequence. The mixture became faint yellow homogeneously after shaking on an oscillator. Then, 1 mL of deionized water was injected into the centrifuge tube. The faint yellow mixture was dissolved in deionized water under ultrasound treatment for 3 h, forming a brown solution. The solution was then added to 1 g of γ-Al₂O₃ powder. The mixture was shaken on an

oscillator and treated under ultrasound treatment for another 1 h. After impregnation, the brown slurry was dried at 100 °C for 12 h and then calcinated at 600 °C in a muffle furnace for 6 h.

Synthesis of MoAl. MoO₃/Al₂O₃ catalyst was defined as MoAl. MoAl was also synthesized by the facile impregnation method. Typically, 0.1635 g of (NH₄)₆Mo₇O₂₄·4H₂O (precursor of MoO₃) and 2 mL of deionized water were loaded in a 10-mL disposable centrifuge tube. (NH₄)₆Mo₇O₂₄·4H₂O was dissolved in deionized water under ultrasound treatment for 1 h, forming a colorless solution. The solution was then added to 1 g of γ-Al₂O₃ powder. The mixture was shaken on an oscillator and treated under ultrasound treatment for another 1 h. After impregnation, the brown slurry was dried at 100 °C for 12 h and then calcinated at 600 °C in a muffle furnace for 6 h.

Characterization

X-ray diffraction (XRD) patterns were carried out on a Bruker D8 Focus operated at 40 kV and 40 mA equipped with graphite filtered Cu K α radiation ($\lambda = 1.5406 \text{ \AA}$) with 2θ values from 20° to 70°.

Raman spectroscopy was performed on a Renishaw inVia reflex Raman spectrometer using a 532 nm Ar ion laser beam under ambient conditions.

Scanning electron microscopy (SEM) was characterized on Hitachi S-4800 under 5 kV. Transmission electron microscopy (TEM) measurements were performed on a JEM-2100F transmission electron microscope under 100 kV. AC-HAADF-STEM measurements were carried out on a JEM ARM 200F from JEOL operated at 200 kV.

The X-ray absorption spectra (XAS) data at Mo and Fe K-edge were collected at BL14W1 station in Shanghai Synchrotron Radiation Facility (SSRF). The electron storage ring was operated at 3.5 GeV with a maximum current of 250 mA. The data were collected at room temperature in a fluorescence excitation mode. All samples were pelletized as disks of 13 mm diameter with 1 mm thickness.

X-ray photoelectron spectroscopy (XPS) was recorded on a PerkinElmer PHI 1600 ESCA instrument with an Al K α X-ray source ($h\nu = 1486.6 \text{ eV}$). The binding energies were calibrated by the C 1s peak at 284.5 eV.

O₂ temperature-programmed oxidation (O₂-TPO) was performed on the Micromeritics Auto Chem II 2920 chemisorption apparatus. Typically, 100 mg of the spent catalysts were heated in a U-type reactor at 300 °C for 1 h under Ar flow and then cooled to 100 °C. The pretreated samples were heated to 700 °C at a rate of 10 °C/min in a mixture of 10 vol% O₂ in He (30 mL/min)

NH₃ temperature-programmed desorption (NH₃-TPD) was also performed on the Micromeritics Auto Chem II 2920 chemisorption apparatus. Typically, 100 mg of the redox catalysts were heated in a U-type reactor at 300 °C for 1 h under Ar flow and then cooled to 100 °C. NH₃ was adsorbed using a flow of 5 vol% NH₃ in He (20 mL/min) for 1 h. Finally, the samples were heated to 700 °C at a rate of 10 °C/min under the flow of He (30 mL/min).

H₂ temperature-programmed reduction (H₂-TPR) was also performed on the Micromeritics Auto Chem II 2920 chemisorption apparatus. Typically, 100 mg of the redox catalysts were heated in a U-type reactor at 300 °C for 1 h under Ar flow and then cooled to 80 °C. Finally, the samples were heated to 800 °C at a rate of 10 °C/min in a mixture of 10 vol% H₂ in Ar (30 mL/min).

C₃H₈ temperature-programmed reduction (C₃H₈-TPR) was measured on the same apparatus, and the output gas products were analyzed on Hiden QIC-20 mass spectrometer (C₃H₈, C₃H₆, CO₂, CH₄, H₂, and H₂O, m/e equals to 29, 41, 44, 16, 2 and 18, respectively). Typically, 100 mg of the redox catalysts were heated in a U-type reactor at 300 °C for 1 h under Ar flow and cooled to 80 °C. The pretreated samples were then heated to 600 °C at a rate of 10 °C/min in a mixture of 15 vol% C₃H₈ in He (10 mL/min).

C_3H_8 - D_2 temperature-programmed surface reduction (C_3H_8 - D_2 -TPSR) was measured on the same apparatus, and the output gas products were analyzed on Hiden QIC-20 mass spectrometer (C_3H_8 , C_3H_7D , D_2 , H_2 , and HD , m/e equals to 29, 30, 4, 2 and 3, respectively). Typically, 100 mg of the redox catalysts were heated in a U-type reactor at 300 °C for 1 h under Ar flow and cooled to 50 °C. The pretreated samples were heated to 600 °C at a rate of 10 °C/min in a mixture of 5 vol% C_3H_8 , 5 vol% D_2 in He (10 mL/min).

C_3H_8 isothermal and pulse experiments were also carried out on the same apparatus, and the output products were also measured on Hiden QIC-20 mass spectrometer (C_3H_8 , C_3H_6 , CO_2 , CH_4 , H_2 , and H_2O , m/e equals to 29, 41, 44, 16, 2 and 18, respectively). Typically, 100 mg samples were pretreated in a U-type reactor at 570 °C for 30 minutes under Ar flow. C_3H_8 was then injected into the reactor for 1 h. The exhausted gas was analyzed by an online mass spectrometer.

In situ diffuse reflectance infrared Fourier transform spectroscopy (in situ DRIFTS) was conducted on a Thermo Scientific Nicolet ISSO spectrometer equipped with a Harrick Scientific DRIFT cell and a mercury-cadmium-telluride MCT detector cooled by liquid N_2 .

C_3H_8 -DRIFTS. The redox catalysts were heated at 570 °C for 30 minutes under Ar flow and then cooled to 50 °C. Background spectra were recorded at the desired temperature. Sample spectra were collected every 50 °C from 50 to 570 °C. The pretreated samples were kept in a mixture of 15 vol% C_3H_8 in He (10 mL/min) for 4 minutes at all temperatures. Background spectra were subtracted simultaneously to obtain the desired IR spectra.

N_2 -DRIFTS. To verify the consecutively out-diffusion of lattice oxygen, the spent 1Mo9FeAl redox catalyst was heated under N_2 flow at the reaction temperature. The spent 1Mo9FeAl redox catalyst experienced the C_3H_8 -DRIFTS experiment was quickly cooled to 50 °C and the spectrum was recorded. The sample was then kept under N_2 (20 mL/min) flow for another 1 h and warmed to 570 °C. The spectrum was collected after being heated under N_2 at 570 °C for 10 minutes. The sample was then quickly cooled to 50 °C, and the spectrum was also recorded.

NH_3 -DRIFTS. Catalysts to be measured were pretreated at 400 °C for 30 minutes under Ar flow to remove the absorbed water and gas and cooled to 50 °C. Background spectra were then recorded. A mixture of 10 vol% NH_3 in He (20 mL/min) was introduced, and sample spectra were collected every minute. Background spectra were subtracted to obtain the desired IR spectra.

Thermal gravity analyses were operated on Setaram Themys thermogravimetry apparatus. 30 mg of the redox catalysts were heated in the suspended crucible at 570 °C for 30 minutes under Ar flow. A mixture of 15 vol% C_3H_8 or C_3H_6 in He (50 mL/min) was then introduced, and the TG profiles were recorded at 570 °C for 1 h.

In situ Raman spectroscopy was performed on a Horiba LabRAM HR Evolution Raman spectrometer using a 532 nm Ar ion laser beam. Raman spectra were recorded from 50 to 570 °C every 50 °C in the flow of 15 vol% C_3H_8 in He (20 mL/min) after pretreated at 300 °C for 2 h to remove the influence of hydrated species.

In situ XRD experiments were operated on a Rigaku Smartlab operated at 60 kV and 220 mA equipped with graphite filtered Cu K α radiation ($\lambda = 1.5406 \text{ \AA}$) with 2θ values from 20° to 70° at a scan speed of 10 °/min. XRD patterns were collected from 50 to 570 °C every 50 °C in the flow of 15 vol% C_3H_8 in He (20 mL/min) after being pretreated at 300 °C for 2 h.

Kinetics experiments

Reduction kinetics experiments of the as-prepared redox catalysts were operated on Setaram Themys thermogravimetry apparatus for quantifying the weight change of the redox catalysts. Typically, 20 mg of the redox catalysts with an average radius of 200 μm was heated at 570 °C under the flow of 2 vol% C_3H_8 in N_2 for 90 minutes. To remove the external and internal mass transfer limitation, the kinetics

experiments were operated at high gas flow rates (100 mL/min), and the detailed calculation can be found in Supplementary Table 13.

To eliminate the buoyancy and drag effects, the reduction kinetics experiments were conducted with a blank experiment using the blank crucible at the same reaction conditions. The solid conversion X was calculated using the corrected sample weight based on Eq. 1.

$$X = \frac{m_0 - m_t}{m_0 - m_\infty} \quad (1)$$

Where the m_0 represents the weight of the fresh sample, m_t is the weight at time t during the reduction, m_∞ is the ultimate mass of the sample at the end of the reduction; bulk diffusion coefficient, D , and oxygen surface exchange coefficient, k .

External and internal mass transfer limitations were eliminated by increasing the gas flow rates based on the Mears criterion and the Weisz–Prater criterion.

The external mass transfer limitation was excluded if the Mears number calculated from Eq. 2 is less than 0.15.

$$MR = \frac{-r'_{C_3H_8,obs}(1-\phi)\rho_{1Mo9FeAl}\left(\frac{D}{2}\right)^n}{k_c C_{C_3H_8,b}} \quad (2)$$

where $-r'_{C_3H_8,obs}$ (mol/g-cat s) is the observed reduction rate under C_3H_8 - N_2 flow, $\rho_{1Mo9FeAl}$ is the solid density of 1Mo9FeAl, ϕ is the porosity of 1Mo9FeAl, D is the diameter of 1Mo9FeAl particle, n is the reaction order of C_3H_8 , k_c is the mass transfer coefficient of C_3H_8 in N_2 , and $C_{C_3H_8,b}$ is the bulk concentration of C_3H_8 .

The internal mass transfer limitation was eliminated if the Weisz–Prater parameter calculated from Eq. 3 is significantly less than 1.

$$C_{WP} = \frac{-r'_{C_3H_8,obs}\rho_{1Mo9FeAl}\left(\frac{D}{2}\right)^2}{D_{eff}C_{C_3H_8,s}} \quad (3)$$

where D_{eff} is the effective diffusivity of C_3H_8 in N_2 and $C_{C_3H_8,s}$ is the concentration of C_3H_8 at the surface of 1Mo9FeAl particle.

Supplementary Table 13 presented the detailed parameters involved in the calculation for MR and C_{WP} in determining the external and internal mass transfer limitation. Based on the calculation results, both external and internal mass transfer limitation was eliminated in this work.

Redox test

Redox tests were carried out in a fixed-bed reactor equipped with a quartz tube (8 mm inner diameter and 24 cm length) at 0.14 MPa. Typically, 0.5 g of as-prepared 1MoxFeAl redox catalysts (20–40 mesh) diluted with 1 mL of quartz particles was loaded in the quartz tubular reactor. Prior to the reduction period, the sample was heated to 570 °C under flowing nitrogen (17 mL/min). Afterward, 1MoxFeAl was reduced in the mixture of propane (4 mL/min) and nitrogen (17 mL/min). The Gas Hour Space Velocity (GHSV) was about 3000 h^{-1} . During the switching between propane and air flows (switch over between the reduction and regeneration period), an inert period (nitrogen only, 17 mL/min) of about 10 minutes was essential to avoid direct contact between propane and air. After heating in air for regeneration at 570 °C, one redox cycle was completed. The time for reduction, regeneration, and inert period was set to be 4, 10, and 10 minutes, respectively. The stability test was performed over 1Mo9FeAl for 300 redox cycles.

The outlet gas was analyzed by an online GC (2060) equipped with a flame ionization detector (Chromosorb 102 column) and a thermal conductivity detector (Al_2O_3 Plot column) and GC (Micro GC 490, Agilent) equipped with three channels (MS 5A Plot column, Pora Plot Q, and PoraPlot Q). The instantaneous propane conversion and

gas phase products selectivity was determined from Eq. 4 and Eq. 5

$$\text{Con (\%)} = 100 * \frac{[\text{F}_{\text{C}_3\text{H}_8}]_{\text{inlet}} - [\text{F}_{\text{C}_3\text{H}_8}]_{\text{outlet}}}{[\text{F}_{\text{C}_3\text{H}_8}]_{\text{inlet}}} \quad (4)$$

$$\text{Sel (\%)} = 100 * n_i * \frac{[\text{F}_i]_{\text{outlet}}}{\sum n_i * [\text{F}_i]_{\text{outlet}}} \quad (5)$$

The total selectivity of product *i* based on all products was calculated from Eq. 6.

$$\text{Sel (\%)} = 100 * n_i * \frac{[\text{F}_i]_{\text{outlet}}}{[\text{F}_{\text{C}_3\text{H}_8}]_{\text{inlet}} - [\text{F}_{\text{C}_3\text{H}_8}]_{\text{outlet}}} \quad (6)$$

The instantaneous propylene productivity was calculated on the basis of Eq. 7, and the accumulative yield of propylene within 10 minutes during the dehydrogenation stage was determined from Eq. 8.

$$\text{Productivity} = \frac{[\text{F}_{\text{C}_3\text{H}_6}]_{\text{outlet}}}{m} \quad (7)$$

$$\text{Yield} = \int \text{Productivity} dt \quad (8)$$

The accumulative conversion (Eq. 9) and selectivity (Eq. 10) within *t* minutes were defined as the integral conversion and selectivity in Eqs. 2 and 3 dividing *t* minutes during the dehydrogenation stage.

$$\text{Con}_{\text{int}} (\%) = \frac{\int \text{Con (\%)} dt}{t} \quad (9)$$

$$\text{Sel}_{\text{int}} (\%) = \frac{\int \text{Sel (\%)} dt}{t} \quad (10)$$

i = component *i* in exhausted gases; n_i = number of carbon atoms of component *i*; $[\text{F}_i]_{\text{outlet}}$ = molar flow rate of component *i* out of reactor (mol/h); $[\text{F}_{\text{C}_3\text{H}_6}]_{\text{outlet}}$ = molar flow of propylene out of reactor (mol/h); $[\text{F}_{\text{C}_3\text{H}_8}]_{\text{outlet}}$ = molar flow of propane out of reactor (mol/h); $[\text{F}_{\text{C}_3\text{H}_8}]_{\text{inlet}}$ = molar flow of propane in of reactor (mol/h); *t* = the time during the dehydrogenation stage (minute); *m* = weight of the redox catalysts.

Based on the internal standard experiments, trace coking or tar was formed under the reduction stage, taking the carbon balance into consideration. To calculate the propylene yields, a carbon mass balance was adopted to calculate the conversion and selectivity.

Data availability

The data generated in this study are provided in Supplementary Information and Source Data file. Source data are provided with this paper.

References

- Sattler, J. J. H. B., Ruiz-Martinez, J., Santillan-Jimenez, E. & Weckhuysen, B. M. Catalytic dehydrogenation of light alkanes on metals and metal oxides. *Chem. Rev.* **114**, 10613–10653 (2014).
- Otroshchenko, T., Jiang, G., Kondratenko, V. A., Rodemerck, U. & Kondratenko, E. V. Current status and perspectives in oxidative, non-oxidative and CO₂-mediated dehydrogenation of propane and isobutane over metal oxide catalysts. *Chem. Soc. Rev.* **50**, 473–527 (2020).
- Chen, S., Pei, C., Sun, G., Zhao, Z. -J. & Gong, J. Nanostructured catalysts toward efficient propane dehydrogenation. *Acc. Mater. Res.* **1**, 30–40 (2020).
- Chen, S. et al. Propane dehydrogenation: catalyst development, new chemistry, and emerging technologies. *Chem. Soc. Rev.* **50**, 3315–3354 (2021).
- Zhao, Z. -J. et al. Hydroxyl-mediated non-oxidative propane dehydrogenation over VO_x/γ-Al₂O₃ catalysts with improved stability. *Angew. Chem. Int. Ed. Engl.* **57**, 6791–6795 (2018).
- Zhao, D. et al. In situ formation of ZnO_x species for efficient propane dehydrogenation. *Nature* **599**, 234–238 (2021).
- Yan, H. et al. Tandem In₂O₃-Pt/Al₂O₃ catalyst for coupling of propane dehydrogenation to selective H₂ combustion. *Science* **371**, 1257–1260 (2021).
- Huš, M., Kopač, D., Bajec, D. & Likozar, B. Effect of surface oxidation on oxidative propane dehydrogenation over chromia: an ab initio multiscale kinetic study. *ACS Catal.* **11**, 11233–11247 (2021).
- Gao, D., Li, W., Wang, H., Wang, G. & Cai, R. Heterogeneous catalysis for CO₂ conversion into chemicals and fuels. *Trans. Tianjin Univ.* **28**, 245–264 (2022).
- Kopač, D., Jurković, D. L., Likozar, B. & Huš, M. First-principles-based multiscale modelling of nonoxidative butane dehydrogenation on Cr₂O₃(0001). *ACS Catal.* **10**, 14732–14746 (2020).
- Kopač, D., Likozar, B. & Huš, M. Metal-doped Cr₂O₃ as a catalyst for non-oxidative propane and butane dehydrogenation: a multiscale kinetic study. *Appl. Surf. Sci.* **575**, 151653 (2022).
- Skubic, L. et al. Ab initio multiscale process modeling of ethane, propane and butane dehydrogenation reactions: a review. *Catalysts* **10**, 1405 (2020).
- Gao, Y. et al. A molten carbonate shell modified perovskite redox catalyst for anaerobic oxidative dehydrogenation of ethane. *Sci. Adv.* **17**, eaaz9339 (2020).
- Chen, S. et al. Modulating lattice oxygen in dual-functional Mo-V-O mixed oxides for chemical looping oxidative dehydrogenation. *J. Am. Chem. Soc.* **141**, 18653–18657 (2019).
- Yusuf, S., Neal, L., Bao, Z., Wu, Z. & Li, F. Effects of sodium and tungsten promoters on Mg₆MnO₈-based core-shell redox catalysts for chemical looping-oxidative dehydrogenation of ethane. *ACS Catal.* **9**, 3174–3186 (2019).
- Wang, C. et al. Near 100% ethene selectivity achieved by tailoring dual active sites to isolate dehydrogenation and oxidation. *Nat. Commun.* **12**, 5447 (2021).
- Zha, S. et al. Predicting the catalytic activity of surface oxidation reactions by ionization energies. *CCS Chem.* **2**, 262–270 (2020).
- Li, Y., Han, S., Zhang, L. & Yu, Y. Manganese-based catalysts for indoor volatile organic compounds degradation with low energy consumption and high efficiency. *Trans. Tianjin Univ.* **28**, 53–66 (2021).
- Wang, D., Jin, L., Li, Y. & Hu, H. Upgrading of heavy oil with chemical looping partial oxidation over M²⁺ doped Fe₂O₃. *Energy Fuels* **33**, 257–265 (2018).
- Qin, L. et al. Impact of 1% lanthanum dopant on carbonaceous fuel redox reactions with an iron-based oxygen carrier in chemical looping processes. *ACS Energy Lett.* **2**, 70–74 (2017).
- Liu, Y. et al. Near 100% CO selectivity in nanoscaled iron-based oxygen carriers for chemical looping methane partial oxidation. *Nat. Commun.* **10**, 5503 (2019).
- Novotný, P., Yusuf, S., Li, F. & Lamb, H. H. Oxidative dehydrogenation of ethane using MoO₃/Fe₂O₃ catalysts in a cyclic redox mode. *Catal. Today* **317**, 50–55 (2018).
- Sun, Y. -N., Tao, L., You, T., Li, C. & Shan, H. Effect of sulfation on the performance of Fe₂O₃/Al₂O₃ catalyst in catalytic dehydrogenation of propane to propylene. *Chem. Eng. J.* **244**, 145–151 (2014).
- Jeong, M. H., Sun, J. Young Han, G., Lee, D. H. & Bae, J. W. Successive reduction-oxidation activity of FeO_x/TiO₂ for

- dehydrogenation of ethane and subsequent CO₂ activation. *Appl. Catal. B Environ.* **270**, 118887 (2020).
25. Brookes, C. et al. Molybdenum oxide on Fe₂O₃ core-shell catalysts: probing the nature of the structural motifs responsible for methanol oxidation catalysis. *ACS Catal.* **4**, 243–250 (2013).
 26. Brookes, C. et al. The nature of the molybdenum surface in iron molybdate. The active phase in selective methanol oxidation. *J. Phys. Chem. C.* **118**, 26155–26161 (2014).
 27. Ji, Z., Lv, H., Pan, X. & Bao, X. Enhanced ethylene selectivity and stability of Mo/ZSM5 upon modification with phosphorus in ethane dehydrogenation. *J. Catal.* **361**, 94–104 (2018).
 28. Abello, M. C., Gomez, M. F. & Ferretti, O. Mo/ γ -Al₂O₃ catalysts for the oxidative dehydrogenation of propane: effect of Mo loading. *Appl. Catal. A Gen.* **207**, 421–431 (2001).
 29. Harlin, M. E., Backman, L. B., Krause, A. O. I. & Jylhä, O. J. T. Activity of molybdenum oxide catalyst in the dehydrogenation of *n*-butane. *J. Catal.* **183**, 300–313 (1999).
 30. Chen, K., Xie, S., Bell, A. T. & Iglesia, E. Structure and properties of oxidative dehydrogenation catalysts based on MoO₃/Al₂O₃. *J. Catal.* **198**, 232–242 (2001).
 31. Christodoulakis, A., Heracleous, E., Lemonidou, A. & Boghosian, S. An operando Raman study of structure and reactivity of alumina-supported molybdenum oxide catalysts for the oxidative dehydrogenation of ethane. *J. Catal.* **242**, 16–25 (2006).
 32. Novotny, P., Yusuf, S., Li, F. & Lamb, H. H. MoO₃/Al₂O₃ catalysts for chemical-looping oxidative dehydrogenation of ethane. *J. Chem. Phys.* **152**, 044713 (2020).
 33. Wang, Y. et al. Controlled synthesis of Fe₃O₄@C@manganese oxides (MnO₂, Mn₃O₄ and MnO) hierarchical hollow nanospheres and their superior lithium storage properties. *Electrochim. Acta* **337**, 135739 (2020).
 34. Guo, Q. et al. Fe₃O₄-CNTs nanocomposites: inorganic dispersant assisted hydrothermal synthesis and application in lithium ion batteries. *J. Solid State Chem.* **213**, 104–109 (2014).
 35. Strobel, R. & Pratsinis, S. E. Direct synthesis of maghemite, magnetite and wustite nanoparticles by flame spray pyrolysis. *Adv. Powder Technol.* **20**, 190–194 (2009).
 36. Ramos Guivar, J. A. et al. Vacancy ordered γ -Fe₂O₃ nanoparticles functionalized with nanohydroxyapatite: XRD, FTIR, TEM, XPS and Mössbauer. *Stud. Appl. Surf. Sci.* **389**, 721–734 (2016).
 37. Ni, Y., Ge, X., Zhang, Z. & Ye, Q. Fabrication and characterization of the plate-shaped γ -Fe₂O₃ nanocrystals. *Chem. Mater.* **14**, 1048–1052 (2002).
 38. Li, Y. K., Zhang, G., Lu, W. T. & Cao, F. F. Amorphous Ni-Fe-Mo suboxides coupled with Ni network as porous nanoplate array on nickel foam: a highly efficient and durable bifunctional electrode for overall water splitting. *Adv. Sci.* **7**, 1902034 (2020).
 39. Wang, S. et al. Molecular structure of molybdate adsorption on goethite at pH 5–8: a combined DFT + U, EXAFS, and ab initio XANES study. *J. Phys. Chem. C.* **125**, 22052–22063 (2021).
 40. Xin, Y. et al. Active site identification and modification of electronic states by atomic-scale doping to enhance oxide catalyst innovation. *ACS Catal.* **8**, 1399–1404 (2018).
 41. Subba Reddy, C. V., Walker, E. H. & Wen, C. & Mho, S. -i. Hydrothermal synthesis of MoO₃ nanobelts utilizing poly(ethylene glycol). *J. Power Sources* **183**, 330–333 (2008).
 42. El Mendili, Y. et al. New evidences of in situ laser irradiation effects on γ -Fe₂O₃ nanoparticles: a Raman spectroscopic study. *J. Raman Spectrosc.* **42**, 239–242 (2011).
 43. Varadwaj, K. S. K., Panigrahi, M. K. & Ghose, J. Effect of capping and particle size on Raman laser-induced degradation of γ -Fe₂O₃ nanoparticles. *J. Solid State Chem.* **177**, 4286–4292 (2004).
 44. Babay, S., Mhiri, T. & Toumi, M. Synthesis, structural and spectroscopic characterizations of maghemite γ -Fe₂O₃ prepared by one-step coprecipitation route. *J. Mol. Struct.* **1085**, 286–293 (2015).
 45. Uhlrich, J. J. et al. Preparation and characterization of iron-molybdate thin films. *Surf. Sci.* **605**, 1550–1555 (2011).
 46. Tsilomelekis, G. & Boghosian, S. On the configuration, molecular structure and vibrational properties of MoO_x sites on alumina, zirconia, titania and silica. *Catal. Sci. Technol.* **3**, 1869 (2013).
 47. Cui, H., Liu, Y. & Ren, W. Structure switch between α -Fe₂O₃, γ -Fe₂O₃ and Fe₃O₄ during the large scale and low temperature sol-gel synthesis of nearly monodispersed iron oxide nanoparticles. *Adv. Powder Technol.* **24**, 93–97 (2013).
 48. Yamashita, T. & Hayes, P. Analysis of XPS spectra of Fe²⁺ and Fe³⁺ ions in oxide materials. *Appl. Surf. Sci.* **254**, 2441–2449 (2008).
 49. Jiang, F. et al. Propane dehydrogenation over Pt/TiO₂-Al₂O₃ catalysts. *ACS Catal.* **5**, 438–447 (2014).
 50. Narayanan, S., Sultana, A., Le, Q. T. & Auroux, A. A comparative and multitechnical approach to the acid character of templated and non-templated ZSM-5 zeolites. *Appl. Catal. A Gen.* **168**, 373–384 (1998).
 51. Lietti, L. et al. Characterization and reactivity of V₂O₅-MoO₃/TiO₂ De-NO_x SCR catalysts. *J. Catal.* **187**, 419–435 (1999).
 52. Lin, S. D., Gluhoi, A. C. & Nieuwenhuys, B. E. Ammonia oxidation over Au/MO/ γ -Al₂O₃-activity, selectivity and FTIR measurements. *Catal. Today* **90**, 3–14 (2004).
 53. Davydov, A. A. *Infrared Spectroscopy of Adsorbed Species on the Surface of Transition Metal Oxides* (Wiley, 1990).
 54. Matralis, H. K., Ciardelli, M., Ruwet, M. & Grange, P. Vanadia catalysts supported on mixed TiO₂-Al₂O₃ supports: effect of composition on the structure and acidity. *J. Catal.* **157**, 368–379 (1995).
 55. Qi, G. & Yang, R. Characterization and FTIR studies of MnO_x-CeO₂ catalyst for low-temperature selective catalytic reduction of NO with NH₃. *J. Phys. Chem. B* **108**, 15738–15747 (2004).
 56. Jia, Y. et al. Insight into the reaction mechanism over PMoA for low temperature NH₃-SCR: a combined In-situ DRIFTS and DFT transition state calculations. *J. Hazard. Mater.* **412**, 125258 (2021).
 57. Nagasaki, Y. -h, Tamura, M., Yabushita, M., Nakagawa, Y. & Tomishige, K. Dehydration of amides to nitriles over heterogeneous silica-supported molybdenum oxide catalyst. *ChemCatChem* **14**, e202101846 (2022).
 58. Husnain, N., Wang, E., Fareed, S. & Tuoqeer Anwar, M. Comparison on the low-temperature NH₃-SCR performance of γ -Fe₂O₃ catalysts prepared by two different methods. *Catalysts* **9**, 1018 (2019).
 59. Liu, J., Shi, X., Liu, H., Dong, L. & Li, B. Study on the performance of magnetic Co₃O₄/ γ -Fe₂O₃ catalyst in NO + CO reaction. *Appl. Surf. Sci.* **533**, 147498 (2020).
 60. Yang, S. et al. Improvement of the activity of γ -Fe₂O₃ for the selective catalytic reduction of NO with NH₃ at high temperatures: NO reduction versus NH₃ oxidization. *Ind. Eng. Chem. Res.* **52**, 5601–5610 (2013).
 61. Shi, X. et al. Mn-modified CuO, CuFe₂O₄, and γ -Fe₂O₃, three-phase strong synergistic coexistence catalyst system for NO reduction by CO with a wider active window. *ACS Appl. Mater. Inter.* **10**, 40509–40522 (2018).
 62. Gao, M., Li, W., Dong, J., Zhang, Z. & Yang, B. Synthesis and characterization of superparamagnetic Fe₃O₄@SiO₂ core-shell composite nanoparticles. *World J. Cond. Matter Phys.* **01**, 49–54 (2011).
 63. Ni, S. et al. Hydrothermal synthesis of Fe₃O₄ nanoparticles and its application in lithium ion battery. *Mater. Lett.* **63**, 2701–2703 (2009).
 64. Shebanova, O. N. & Lazor, P. Raman study of magnetite (Fe₃O₄): laser-induced thermal effects and oxidation. *J. Raman Spectrosc.* **34**, 845–852 (2003).
 65. Chicot, D. et al. Mechanical properties of magnetite (Fe₃O₄), hematite (α -Fe₂O₃) and goethite (α -FeOOH) by instrumented indentation and molecular dynamics analysis. *Mater. Chem. Phys.* **129**, 862–870 (2011).
 66. Tsilomelekis, G. & Boghosian, S. An operando Raman study of molecular structure and reactivity of molybdenum (VI) oxide

- supported on anatase for the oxidative dehydrogenation of ethane. *Phys. Chem. Chem. Phys.* **14**, 2216–2228 (2012).
67. Liu, Z., Zhang, S., Li, J. & Ma, L. Promoting effect of MoO₃ on the NO_x reduction by NH₃ over CeO₂/TiO₂ catalyst studied with in situ DRIFTS. *Appl. Catal. B Environ.* **144**, 90–95 (2014).
68. Tian, Y., Dudek, R. B., Westmoreland, P. R. & Li, F. Effect of sodium tungstate promoter on the reduction kinetics of CaMn_{0.9}Fe_{0.1}O₃ for chemical looping–oxidative dehydrogenation of ethane. *Chem. Eng. J.* **398**, 125583 (2020).
69. Knoblauch, N., Dorrer, L., Fielitz, P., Schmucker, M. & Borchardt, G. Surface controlled reduction kinetics of nominally undoped polycrystalline CeO₂. *Phys. Chem. Chem. Phys.* **17**, 5849–5860 (2015).

Acknowledgements

We acknowledge the National Key R&D Program of China (2021YFA1501302), the National Natural Science Foundation of China (No. 22121004, U20B6002, 22122808), the Haihe Laboratory of Sustainable Chemical Transformations and the Program of Introducing Talents of Discipline to Universities (BP0618007) for financial support. This work is supported by the XPLOER PRIZE.

Author contributions

J.L.G. supervised the project. X.H.W. performed the experiment and characterization. X.H.W., C.L.P., Z.-J.Z., and J.L.G. designed the project. S.C., G.D.S., W.W., and X.H.Z. contributed to the characterization of the redox catalysts. H.B.S. and J.C.S. contributed to the kinetic analysis. X.Y.L. and X.C. contributed to useful discussion. All the authors contributed to the writing of the manuscript.

Competing interests

The authors declare no competing interests.

Additional information

Supplementary information The online version contains supplementary material available at <https://doi.org/10.1038/s41467-023-37818-w>.

Correspondence and requests for materials should be addressed to Jinlong Gong.

Peer review information *Nature Communications* thanks the anonymous reviewers for their contribution to the peer review of this work.

Reprints and permissions information is available at <http://www.nature.com/reprints>

Publisher's note Springer Nature remains neutral with regard to jurisdictional claims in published maps and institutional affiliations.

Open Access This article is licensed under a Creative Commons Attribution 4.0 International License, which permits use, sharing, adaptation, distribution and reproduction in any medium or format, as long as you give appropriate credit to the original author(s) and the source, provide a link to the Creative Commons license, and indicate if changes were made. The images or other third party material in this article are included in the article's Creative Commons license, unless indicated otherwise in a credit line to the material. If material is not included in the article's Creative Commons license and your intended use is not permitted by statutory regulation or exceeds the permitted use, you will need to obtain permission directly from the copyright holder. To view a copy of this license, visit <http://creativecommons.org/licenses/by/4.0/>.

© The Author(s) 2023